

# **Flexural strength and defect behaviour of polygranular graphite under different states of stress**

M. Mostafavi <sup>1,\*</sup>, S.A. McDonald <sup>2</sup>, H. Çetinel <sup>1,3</sup>, P.M. Mummery <sup>4</sup>, T.J. Marrow <sup>1</sup>

<sup>1</sup> Department of Materials, The University of Oxford, Parks Road, Oxford, OX1 3PH, UK

<sup>2</sup> School of Materials, The University of Manchester, Oxford Road, Manchester, M13 9PL, UK

<sup>3</sup> Department of Mechanical Engineering, Celâl Bayar University, Muradiye Campus, 45140, Manisa, Turkey

<sup>4</sup> School of Mechanical, Civil and Aerospace Engineering, The University of Manchester, Sackville Street, Manchester, M13 9PL, UK

## **Abstract**

The effect of stress state on the fracture behaviour of Gilsocarbon, an isotropic nuclear grade polygranular graphite, has been studied by employing four-point bend and ring-on-ring loading configurations to achieve uniaxial and equi-biaxial flexural stress states respectively. Optical images of the specimens' tensile surface were analysed by digital image correlation to measure the full-field displacements: these were used to identify the fracture initiation sites, analyse crack geometry (surface length and opening displacements) and also to calculate the  $J$ -integral strain energy release rate associated with surface crack propagation. Surface cracks that did not propagate to failure were identified and subsequently examined by X-ray computed

---

\* Corresponding author Tel: +44 (0) 1865 283326 Fax: +44 (0) 1865 273789 E-mail: [mahmoud.mostafavi@materials.ox.ac.uk](mailto:mahmoud.mostafavi@materials.ox.ac.uk) (Mahmoud Mostafavi)

tomography combined with digital volume correlation: measurements were made of their three-dimensional displacement fields when subjected to an opening tensile stress using a modified (flat) Brazilian Disk test geometry. The crack opening behaviour is explained by an effect of stress state on the development of the crack tip fracture process zone, which is in agreement with the effect of stress state on the measured strain energy release rates of sub-critical crack propagation. Both are attributed to the plastic constraint effect, which varies with the stress state in materials that can undergo inelastic deformation.

## **Nomenclature and Initialisations**

$a$	Crack depth
$c$	Half crack length
$da$	Crack growth
$h$	Specimen height
$i$	Number of the specimen, ranked by the fracture load from minimum ( $i=1$ ) to maximum ( $i=N$ )
$m$	Weibull modulus
$t$	Specimen thickness
$x, y, z$	Cartesian coordinates: $y$ (vertical direction) is the crack propagation direction; $x$ (horizontal direction) is in-plane direction perpendicular to crack propagation; $z$ is through the thickness
$E$	Elastic modulus

$J$	$J$ -integral
$J_c$	Critical (fracture) $J$ -integral
$K_{Ic}$	Critical (fracture) mode I stress intensity factor
$N$	Total number of tested specimens
$P$	Applied load
$P_c$	Critical (fracture) load
$R$	Radius of the specimen in the ring-on-ring configuration
$R_i$	Radius of the inner ring in ring-on-ring configuration
$R_o$	Radius of the outer ring in ring-on-ring configuration
$S_i$	Inner span in four-point-bend configuration
$S_o$	Outer span in four-point-bend configuration
$V_x$	Displacement (in the horizontal $x$ -direction)
$V_y$	Displacement (in the vertical $y$ -direction)
$W$	Specimen width
$\beta$	Biaxiality ratio
$\delta$	Crack mouth opening displacement
$\delta_m$	Average crack opening displacement
$\nu$	Poisson's ratio

$\sigma_b$	Bending stress
$\sigma_w$	Weibull stress
$\Delta V_x$	Change in displacement $V_x$
AGR	Advanced Gas-cooled reactor
CMOD	Crack Mouth Opening Displacement
COD	Crack Opening Displacement (average)
DIC	Digital Image Correlation
DVC	Digital Volume Correlation
EDM	Electro-Discharge Machining
EPRI	Electric Power Research Institute
FBD	Flat Brazilian Disk
FEM	Finite Element Method
FPB	Four-Point Bend
MIXF	Manchester Imaging X-ray Facility
PMMA	Poly(Methyl Methacrylate)
PVC	Polyvinyl Chloride
SED	Strain Energy Density
XCT	X-ray Computed Tomography

# 1 Introduction

Polygranular graphite is a quasi-brittle material. Its unique physical properties lead to use in various structural applications, including neutron moderation in fission reactors such as the UK's gas cooled reactors [1], muon generating targets for high intensity accelerated proton beams [2] and also thermal-shock resistant moulds for continuous casting systems [3]. In such applications, an understanding of the conditions for component failure is needed for design and safe operation. There have been many studies of graphite's fracture properties under uniaxial loading (e.g.[4, 5]), but fewer studies on the effects of stress state (e.g. [6, 7]), despite the fact that many applications impose multi-axial stresses. For example, in graphite components in nuclear reactors the multi-axial stress-state can be either internal stresses due to irradiation-induced dimensional change or external loads from component interactions [8]; stress concentrators such as keyways that act as notches further affect the multi-axiality of stresses [9, 10]). The effect of multi-axial stress can be significant: for graphite with isotropic properties, equi-biaxial loading causes an approximate 20% reduction in flexural strength compared to uniaxial loading [11]. The mechanism for this has not been investigated deeply, in contrast to the well-documented stress biaxiality effect on the fracture of ductile metals that is explained by plastic constraint (e.g. [12]).

The constraint effect on fracture of ductile materials is a significant element in structural integrity assessments, since accounting for constraint may better define the margin between conservative and realistic behaviour [13]. The plastic constraint effect may be explained briefly as follows: fracture toughness can be expressed in terms of a critical strain energy release rate, which is generally considered a material

parameter. However, the measured fracture toughness may be geometry dependent in materials that are capable of dissipating energy through permanent (i.e. plastic or more generally inelastic) deformation. Plastic constraint, defined as the resistance of the specimen against inelastic deformation [14], is employed to explain this phenomenon. The energy release rate required to propagate fracture includes energy dissipated through the inelastic deformation processes that accompany the creation of new surfaces. For metallic materials, the inelastic processes include deformation to nucleate voids for ductile rupture or to debond particles (such as carbides in steel) from the matrix for brittle cleavage. For quasi-brittle materials, of which graphite, concrete, ceramic matrix composites and artificial bone replacements are examples, the equivalent inelastic energy can be due to distributed micro-cracking [15]. These energy dissipation processes occur within the enclave of an inelastic crack tip zone: in metals this is commonly described as the crack tip plastic zone. This inelastic zone mediates between the crack tip and the surrounding elastic strain field, and may thereby affect the condition for fracture propagation in a test specimen or component. A root cause of geometry dependent fracture toughness is neglect of the effect of constraint on inelastic deformation within the calculation of the strain energy release rate for crack propagation in test specimens and components. In ductile metals, a relation between the development of the inelastic zone (i.e. crack tip plastic zone) and constraint may be established [12], and this has been shown to account for the effect of constraint on measured fracture toughness [16]. For materials that are in a condition of small scale yielding, the most commonly used parameter to quantify in-plane constraint is the non-singular term of the asymptotic stress distribution; the  $T$ -stress [17].

Fracture assessment codes for metallic materials (such as R6 [13]) therefore include correction factors, applied to linear elastic calculations, to account for plastic constraint in structural components. This allows data from high constraint test specimens to be applied to lower constraint components: high constraint reduces the measured toughness in ductile metals, so this approach improves confidence in the safety margin of the assessment. The potential effect of plastic constraint is not considered in structural integrity codes for quasi-brittle materials such as graphite [18]; physically-based models for the effects of constraint on inelastic deformation are required for this to be achieved. In addition to improving confidence in the structural integrity assessment of graphite, the development of an approach that addresses constraint effects will benefit the application of other quasi-brittle materials in engineering structures.

The focus of this paper is therefore on an isotropic, nuclear-grade, polygranular graphite: Gilsocarbon; in addition to being technologically important, it is a good model material for quasi-brittle behaviour. This grade of graphite is primarily used as reflector and moderator in UK's Advanced Gas Reactors (AGR). Its porous structure comprises approximately spherical filler particles order of about 0.5 mm in size [19] within a matrix of graphitised pitch and finer filler particles.

This paper reports an experimental study of strength and defects in Gilsocarbon under uniaxial (four-point bend) and equi-biaxial (ring-on-ring) loading. The work contributes to a research programme that aims to understand the effects of component geometries such as stress concentrating notches on their strength: this requires a knowledge of defect behaviour under different states of stress that may be described in terms of constraint. In this work, digital image correlation (DIC) of optical images

has been used to measure the full-field displacements on the specimen tensile surface up to the point of fracture, and thereby the surface lengths and opening displacements of the identified crack nuclei. A method to obtain the strain energy release rate from the experimentally measured displacement fields [20] has been applied to calculate the  $J$ -integral associated with the surface propagation of the crack nuclei. Three-dimensional examination of non-critical cracks that did not propagate to failure has been performed using in situ X-ray computed tomography (XCT) and the digital volume correlation (DVC) to investigate the opening of such non-critical cracks under load and hence their dimensions. The behaviours of crack nuclei in a quasi-brittle material were thereby investigated on their first and subsequent exposure to stresses that were close to fracture. The objectives were to determine whether the stress state affected the development of crack tip deformation and the corresponding energy required for crack propagation, and to consider whether this might be understood in terms of constraint in a manner analogous to ductile materials.

## **2 Two dimensional study of crack nucleation and propagation**

### **2.1 In-situ 2D optical observation**

To obtain statistically significant data, 62 four-point bend and 26 ring-on-ring specimens were tested. The surfaces of the specimens were monitored during loading; the majority of tests (35 uniaxial and 17 biaxial specimens) used a 4 MPixel 14 bit camera recording images at 1 frame per second. The remainder (21 uniaxial and 9 biaxial samples) were observed by a high-speed Photron Fastcam 1024 LRT DVR system (1 MPixel, 10 bit camera) recording images at 125 – 1000 frames per second (fps). The schematics of the uniaxial experiment are illustrated in Figure 1a and that of the equi-biaxial experiment in Figure 1b; the four-point bend specimens



had width ( $W$ )= 200, height ( $h$ )= 200 and thickness ( $t$ )= 10 mm, loaded with inner span ( $S_i$ ) = 90 mm and outer span ( $S_o$ )= 180 mm; the ring-on-ring specimens had diameter ( $2R$ ) = 350 mm with inner span ( $2R_i$ ) = 150 and outer span ( $2R_o$ ) = 300 mm. Details of the specimens, digital image correlation and its calibration were discussed in an earlier paper [21], in which partial data were reported. As these are slender specimens the flexural bending strength,  $\sigma_b$  was calculated using Eq. (1) for uniaxial and Eq. (2) for equi-biaxial loading:

$$\sigma_b = \frac{3P_c(S_o - S_i)}{ht^2} \quad (1)$$

$$\sigma_b = \frac{3(1+\nu)}{2\pi t^2} P_c \left[ \ln\left(\frac{R_o}{R_i}\right) + \frac{(1-\nu)(R_o^2 - R_i^2)}{2(1+\nu)R^2} \right] \quad (2)$$

where  $P_c$  is the fracture load and  $\nu$  is Poisson's ratio. The specimens were ranked and numbered ( $i$ ) based on their strength. The probability of fracture of each ( $P_f$ ) was calculated by:

$$P_f = \frac{i - 0.5}{N} \quad (3)$$

where  $N$  is the total number of the specimens. A two-parameter Weibull distribution was fitted to the flexural strength [22], using Eq. (4). The distributions are shown in Figure 2.

$$P_f = 1 - \exp\left(-\frac{\sigma_b}{\sigma_w}\right)^m \quad (4)$$

where  $\sigma_w$  is the Weibull stress and  $m$  is the Weibull exponent. Under uniaxial load  $\sigma_w = 28.6$  MPa,  $m = 25.3$  and under biaxial load:  $\sigma_w = 23.4$  MPa,  $m = 25.4$ .

## 2.2 Defect characterisation by digital image correlation

The full-field displacements were obtained by digital image correlation applied to the recorded images using the LaVision DaVis Strain Master V. 7.4 software [23]. An analysis with  $256 \times 256$  pixel window size with 0% overlap (2 passes) followed by  $64 \times 64$  pixel window size with 25% overlap (4 passes) was found to obtain best results for digital image correlation, in terms of detection of defects against the background deformation; at smaller window sizes the RMS of strain at locations remote from the identified cracks became significantly greater than the characteristic strains from crack opening. The chosen loading conditions and geometry apply a uniform displacement gradient or constant surface strain [21]: when a crack nucleates its surface opening is considerably greater than the elastic displacements of the areas where there is no crack and the step change in displacement can be observed as an area of very high nominal strain. This can readily be used to monitor initiated cracks (see for more details [24]). Examples of the maximum principal strain field are shown in Figure 3, obtained within 1 second of final failure; the scale has been chosen to show the cracks as white patches (i.e. high strain). In a limited number of tests, such as these examples, more than one crack was observed to nucleate; in other tests just one nucleus was detected, and in some of the experiments observed at 1 frame per second no crack nucleus was detected. However, the high-speed observations (1000

frames per second) always detected a crack nucleus, which subsequently propagated at sub-sonic speeds (from 0.8 to 17.8 m/s) before instability. The development of a sub-critical surface crack prior to unstable fracture is therefore judged to be a characteristic of this material under flexural loading; the lack of observed cracks in the 1 fps tests being attributed to insufficient time-resolution.

The average opening displacement of each crack, during loading, was obtained from the measured displacement field. Two windows on either sides of the crack were selected and the average horizontal displacement of each (i.e.  $x$  axis perpendicular to the crack) was extracted from the DIC data. It has been discussed elsewhere [21] that for the current specimen and crack sizes the calculated opening displacement is insensitive to the location and size of the area from which the average horizontal displacement is calculated, if the measurements are made within 1 mm of the crack (this distance is a function of the material, crack geometry and the specimen loading condition [21]). Windows with a size of  $0.5 \times 0.5$  mm, with their centres located at a distance of 0.5 mm from the crack were therefore used. The deviation between this measurement and that obtained similarly from non-cracked regions under the same stress provides the crack mouth opening displacement (CMOD) (for more details see [24]). This analysis was performed only on samples monitored by the conventional camera, as the load could not be recorded simultaneously with the high-speed camera images.

The CMOD data calculated by this method are presented in Figure 4, which shows a strong sensitivity to the stress state. The average CMOD ( $\delta$ ) of critical cracks ( $\pm$  one standard deviation), measured one second before unstable failure, was  $8.6 \pm 1.8$   $\mu\text{m}$  under uniaxial and  $17.7 \pm 3.9$   $\mu\text{m}$  under equi-biaxial loading.

### 2.3 Fracture resistance curves

The authors have developed a combined DIC and finite element method (FEM) through which the strain energy release rate of a crack can be calculated directly from its displacement field, as a  $J$ -integral [20]. In short, this method allocates a node in a regular FE mesh to the centre of each DIC window, at which the measured displacement vector is known. This provides a pre-solved finite element model from which the  $J$ -integral can be calculated in a straight forward manner by employing the domain integral method [20]. Unlike other methods (e.g. [25]), which make use of the displacement field distribution to optimise a stress intensity factor (i.e. by comparison with the theoretical singularity of the crack tip elastic strain field), this method does not require the crack tip position to be accurately located. This is a significant benefit for quasi-brittle materials, in which a physical macromechanical crack tip cannot be defined: experimental observations of a long crack in polygranular nuclear graphite confirm there is a smooth transition from the open crack through a fracture process zone to the undamaged region [26]. This method has been applied to graphite specimens of different geometries with satisfactory results [24], finding the calculated values are path independent (varying less than 8% in the worst case) where the displacement field outside the inelastic zone is used.

In order to compare the effects of stress state on the criteria for surface crack propagation, the uniaxial and equi-biaxial displacement fields have been analysed to obtain  $J$ -integral values for sub-critical propagating cracks, using the same material properties  $E = 10.9$  GPa and  $\nu = 0.2$  [21]: the  $J$ -integral analysis currently assumes constant elastic moduli, which are those measured at low stress levels. Previous studies in this material [24] observed that the elastic modulus at the specimen surface

decreased as the fracture stress was approached under uniaxial flexure; the modulus was measured during unloading and is consistent with the effects of increasing micro-crack damage. There are no equivalent data for equi-biaxial conditions; however the maximum principal stress has been shown to be the governing parameter for damage [27], so the effect of equi-biaxial stress on the reduction of elastic modulus is assumed to be comparable to that observed for uniaxial stress. The elastic modulus decreased linearly with strain by up to 13% (i.e. the measured compliance increased by 13%) as fracture was approached under uniaxial stress [24] so a 9% reduction in elastic modulus towards the failure stress is estimated for equi-biaxial conditions - the maximum principal stress at failure under equi-biaxial loading is 23.4 MPa, compared to 28.6 MPa under uniaxial stress. The effects of damage on the elastic moduli, close to failure, are therefore judged to be similar in both stress states. It might be argued that damage is anisotropic under uniaxial loading and so should be the change in elastic modulus, whereas the damage and associated modulus change in the equi-biaxial condition would be isotropic. However, an investigation of the fracture toughness of orthotropic polygranular graphite [28] found that using isotropic properties equivalent to the lower value of elastic modulus provided a good estimate of toughness, when compared with an orthotropic analysis. The relative errors in the calculated  $J$ -integral that may arise by assuming a strain and stress state independent isotropic elastic modulus are therefore considered to be sufficiently small for the uniaxial and equi-biaxial fracture resistances to be compared.

The crack growth resistance ( $J$ -Resistance) curves derived by this analysis (Figure 5) reveal a significant difference in the strain energy release rate for cracks propagating under uniaxial and biaxial loading. The error bars in the figure show the maximum to minimum range of  $J$ -integral obtained by different contours, and confirm path-

insensitivity. The calculation method requires a relatively large region around the crack for sufficient contours to establish path-insensitivity of the  $J$ -integral; typically an area of up to 30 mm  $\times$  30 mm is examined, so not all the observed cracks were suitable for the analysis. The initiation  $J$ -integral ( $J_c$ ) was obtained by interpolation of the  $J$ -Resistance curve data at 0.2 mm crack propagation ( $da = 0.2$  mm – this is typical of standards developed for elastic-plastic materials, e.g. see [13], and so is used here for the purpose of comparison). The average initiation toughness is  $J_c = 176 \pm 44$  J/m<sup>2</sup> under uniaxial and  $J_c = 779 \pm 97$  J/m<sup>2</sup> under equi-biaxial stress.

## 2.4 Crack depth estimation from CMOD compliance

For a linear elastic material with a semi-elliptical, long, shallow surface crack ( $c \gg a$  where  $2c$  is the surface crack length and  $a$  is crack depth) the CMOD ( $\delta$ ) is insensitive to crack length and varies linearly with crack depth [21]:

$$\delta \approx 4\sqrt{2}(1-\nu^2)\left(\sigma_b \frac{a}{E}\right) \quad (5)$$

Elastic finite element simulation carried out in a previous investigation [21] showed that Eq. (5) is valid for both uniaxial and equi-biaxial conditions. The crack mouth opening compliance ( $\delta/\sigma_b$ ) therefore provides a measure of the depth of a crack in an elastic material. The measured crack mouth opening tends to increase linearly with applied stress (Figure 4); using these data the average crack mouth opening compliance (and its standard deviation) for uniaxial loading is  $0.31 \pm 0.07$   $\mu\text{m}/\text{MPa}$  and for equi-biaxial it is  $0.75 \pm 0.18$   $\mu\text{m}/\text{MPa}$ : i.e. the average crack mouth opening compliance is 2.4 times greater under equi-biaxial loading compared to uniaxial loading. Applying Eq. (5), the average crack depth obtained under uniaxial load

would be estimated to be  $a = 0.60 \pm 0.11$  mm and under equi-biaxial load  $a = 1.61 \pm 0.30$  mm. The crack depths under uniaxial flexural are consistent with data obtained by similar methods and analysis in a previous study of the same grade of polygranular graphite under uniaxial flexural [21]; they are also of the order of the defects in the microstructure [29] (i.e. pores and calcination cracks), but those obtained from the crack compliance data under equi-biaxial stress in the same material are significantly greater. This inconsistency is studied in the next section.

### **3 Three dimensional study of crack nuclei**

#### **3.1 In-situ Computed X-ray tomography observation**

In some test specimens several sub-critical crack nuclei were observed prior to failure (e.g. crack 3 in Figure 3a and crack 2 in Figure 3b), of which only one subsequently propagated as the critical crack. Preliminary examinations showed that non-critical nuclei could not be observed reliably by post-test microscopy due to the complex microstructure of nuclear graphite and the narrow crack openings. To characterise the crack dimensions, the three-dimensional displacements in response to applied load were measured using X-ray computed tomography and 3D digital image correlation (i.e. digital volume correlation - DVC); the sub-surface crack opening displacements were used to visualise the crack shape. This approach was developed to study the propagation of long cracks within a wedge-loaded chevron notch specimen of polygranular graphite [26].

Two samples, each containing one non-critical crack, were selected from a uniaxial test and an equi-biaxial test after the original specimens had fractured. The uniaxial crack had a compliance of  $0.17 \pm 0.03$   $\mu\text{m}/\text{MPa}$ , and the equi-biaxial crack  $0.35 \pm 0.02$

$\mu\text{m}/\text{MPa}$ , both measured during the first loading of the sample: the crack that developed under equi-biaxial load had a compliance more than twice that of the uniaxial loaded crack. These two cracks are identified in Figure 4 with hollow symbols. It is interesting to note that these defects, which did not develop to propagate by unstable fracture, also did not develop the high values of CMOD that were observed in the other cracks.

Electro-discharge machining (EDM) was used to cut Flat Brazilian Disks (FBD, see Figure 6a) from the fractured specimens using the earlier DIC observations to position the crack along the centreline. The Brazilian disc geometry uses compressive loading along the centreline to create a perpendicular tensile stress, through the Poisson effect, which acts to open the crack. The X-ray computed tomography (XCT) observations were conducted at the Manchester X-ray Imaging Facility (MXIF). The compressive loading rig (manufactured by DEBEN) is equipped with a Perspex tube that is transparent to visual light and X-rays, so that tomographic scans may be obtained while the specimen is under load (Figure 6b): unfortunately, the loading rig does not permit simultaneous optical observation of the test specimen surface. A 320 kV Nikon Metris custom bay laboratory instrument with a  $2000 \times 2000$  pixel detector was used, operating at 80 kV. The resolution was  $17 \mu\text{m}$  per pixel, due to the cone-beam geometry and the minimum sample to detector distance imposed by the loading rig. Each radiograph imaged an area of  $34 \text{ mm} \times 34 \text{ mm}$ ; a standard back-projection algorithm was used to reconstruct the region of interest using 4500 projections. Each specimen was first observed with a low applied load ( $\approx 100 \text{ N}$ ), to reduce sample movement between scans, and then again with a high load of  $8 \text{ kN}$  applied. The load cell has been designed to be accurate within 0.25% of its maximum load ( $10 \text{ kN}$ ), so the uncertainty in the measured load was less than  $25 \text{ N}$ . The load could not be



monitored during tomography, but measurements before and after each 105 minute scan recorded a load relaxation of less than 5%.

### **3.2 Defect characterisation by digital volume correlation**

The tomographs recorded at low and high load were analysed by digital volume correlation (DVC) using the LaVision DaVis v. 8.1.1 [30] software to map their relative deformation. Four passes with an initial window size of  $256 \times 256 \times 256$  voxels with 50% overlap were followed by 4 passes at  $128 \times 128 \times 128$  voxels with 50% overlap, then 6 passes at  $32 \times 32 \times 32$  pixels with 87% overlap for the uniaxial specimen; 50% overlap was used for the biaxial specimen. This was found to give an optimum description of the displacement field, in terms of resolution and uncertainty. As with the DIC results, the crack nuclei could be visualised as regions of high nominal strain; these are shown in Figure 7a and b for uniaxial and c and d for equibiaxial samples using a strain threshold of 0.04. The data are noisy due to the voxel size of  $17 \mu\text{m}$ : this is quite large relative to the microstructure features (pores with low X-ray attenuation) that provide the contrast for digital volume correlation. The average strain ( $\pm$  one standard deviation) in regions remote from the crack was  $0.013 \pm 0.001$ ; this precision is a consequence of the sub-pixel displacement resolution of DVC. The strain visualisation is thus an approximation to the crack shape; nonetheless it is insensitive to the chosen strain threshold (in the range 0.02 to 0.05). This is a characteristic of image correlation visualisation of cracks from their opening displacements [24] and provides confidence in the estimation of the dimensions of the crack-like defect from its opening behaviour. Both defects have irregular shapes of similar size that are shallow and long; if approximated as semi-elliptical features, they have a depth of approximately 0.5 mm ( $a = 0.47$  and  $0.53$ ), and surface length close to

5 mm ( $2c = 4.5 \pm 0.2$  and  $5.9 \pm 0.4$  mm respectively). The earlier DIC analysis of the optical observations of these features during the flexural loading obtained surface lengths of  $4.61 \pm 0.03$  and  $5.93 \pm 0.04$  mm respectively (the uncertainties differ for DVC and DIC due to differences in correlation window and pixel sizes). Due to the low resolution of tomography, the precise relation of the cracks to features in the microstructure is unclear (Figure 7b and d), though the crack depths are of the order of the microstructure length scale.

The analysis to measure the crack opening displacement from the 3D data followed the method applied in 2D. However, in contrast to DIC's two-dimensional interrogation windows, which are confined to the surface of the specimen, each DVC interrogation window measures the average displacement vector in a volume. The smallest window dimension in this analysis is 32 voxels (0.544 mm). Hence, the crack opening displacement (COD) calculated from DVC is an average over a region of the same order as the crack depth; the crack mouth opening displacement at the free surface (i.e. CMOD) cannot be measured. To reduce the errors in the COD measurements, the average horizontal displacement perpendicular to the vertical crack was obtained within volumes of approximately  $0.5 \text{ mm} \times 3 \text{ mm} \times 0.5 \text{ mm}$  ( $x \times y \times z$ ) on either side of the crack, separated by a distance of 0.5 mm (i.e. 32 voxels): the displacement difference between these the two volumes was taken as the COD. The justification for the size and position of these volumes is based on FE simulations of the expected displacement field: this is explained in section **Error! Reference source not found.** The position of the volumes excludes integration windows that might overlap the crack as such windows have high measurement error. The CODs calculated by this method were  $\delta_m = 1.8 \pm 0.2 \text{ } \mu\text{m}$  for the uniaxial crack and  $\delta_m = 2.2 \pm 0.4 \text{ } \mu\text{m}$  for the equi-biaxial crack. The ratios of COD to applied force ( $\delta_m/P_c$ )

were thus 0.23  $\mu\text{m}/\text{N}$  and 0.28  $\mu\text{m}/\text{N}$  respectively: the two cracks have quite similar opening compliance when loaded in this second experiment. This compliance is consistent with their similar dimensions, but contrasts with the significant difference measured on their first loading.

### **3.3 Finite element simulation**

#### *3.3.1 Full model*

Finite element simulations were carried out to investigate the sensitivity of the displacement fields to crack depth and to determine the optimum method to analyse the DVC data. ABAQUS Standard 6.9 was used to produce five different 3D full-models; each contained a semi-elliptical surface crack at its centre with a half surface length  $c = 2.5$  mm (close to that observed in DIC and DVC analyses) and a crack depth of between 0.5 and 2.5 mm (0.5 mm increments). Typical elastic properties of Gilsocarbon polygranular graphite were used: elastic modulus  $E = 10.9$  GPa; Poisson's ratio  $\nu = 0.2$  [29]. The model contained 54480 20-node brick elements: an example of the FE mesh is shown in Figure 8a, with the deformed model shown in Figure 8b. As the main purpose of the FE simulation was to understand how to obtain the crack opening displacement from the DVC analysis, so it was not necessary to simulate the contact with the loading rig.

To compare the FE simulation with the experimental DVC data, the variation of horizontal displacements,  $V_x$ , close to the crack was extracted. As described earlier, to reduce the effect of noise in the DVC measurements, the displacements along the horizontal axis ( $x$ ) that passed through the centre of the crack were averaged using volumes that were approximately 3 mm wide ( $y$ ) and 0.5 mm deep ( $z$ ). A similar volume was used to average the FE model data, and is indicated in Figure 8a. The

results from the FE simulation are presented in Figure 9, which shows a constant average horizontal displacement is obtained from measurements within approximately 0.5 mm of the crack: this average COD is 77% of the actual CMOD. A representative average crack opening displacement can therefore be obtained using experimental data from volumes that are within 0.5 mm of the crack.

However, Figure 9 also shows there is a poor agreement between the displacement profiles measured by DVC and predicted by the FE simulation, shown by the difference between dash-dot red line (full FE model) and dashed green line (DVC measurement). For instance, for a 0.5 mm deep crack the FE simulation obtains a COD to load ratio ( $\delta_m/P_c$ ) of  $1.11 \times 10^{-3} \mu\text{m/N}$ , which is several orders of magnitude lower than the DVC-measured values. The FE simulation assumed uniform load, but stiff specimens are quite sensitive to the effects of small misalignments of loading anvils. Such effects on specimen deformation have been reported in previous DVC analyses of computed tomography data [24]. To improve the FE simulation of the crack opening, a DVC-informed FE sub-model approach was therefore employed that took account of the actual bulk deformation of the specimen.

### 3.3.2 Sub-model

DVC calculates the full-field three-dimensional displacements, and these can be used as boundary conditions of a finite element simulation. A sub-model was created, simulating the part of the specimen on which DVC was carried out. A  $825 \times 825 \times 200$  voxel ( $x \times y \times z$ ) volume was cropped from the dataset. The sub-model had 24540 20-node brick elements; its dimensions were approximately  $14 \text{ mm} \times 14 \text{ mm} \times 3.4 \text{ mm}$  ( $825 \times 825 \times 200$  voxels at  $17 \mu\text{m}$  resolution). The surface on which the crack opened was a free surface: boundary conditions were applied to the other five constrained

surfaces using displacement fields extracted from the DVC dataset; this was done by fitting first order 2D polynomials to the Cartesian displacement vector components of each surface (15 polynomials in total). These were defined in ABAQUS as user-defined fields and applied to the appropriate surfaces of the model as boundary conditions. In each case the correlation coefficient (r-value) between the polynomial and the experimental data was better than 0.83, which suggests a sufficient approximation. The polynomials were calculated using data from the uniaxial specimen: the polynomial fit for the vertical displacement ( $V_y$ ) of the top surface of uniaxial specimen, relative to its bottom surface, had an r-value of 0.88; the r-value for the same polynomial compared to the equivalent displacements for the biaxial specimen was 0.71. Their similarity demonstrates that the same non-uniform loading has occurred, which may be attributed to imperfectly parallel surfaces of the compression rig; the DVC data show these were inclined at a relative angle of  $0.17^\circ$ .

Nine sub-model FE simulations with different crack depths were carried out:  $a = 0.1$  to  $0.9$  mm with constant half crack length  $c = 2.5$  mm. The deformed shape of the model with  $a = 0.5$  mm is shown in Figure 8d, demonstrating that the behaviour of the DVC-informed sub-model is quite different from that of the uniformly loaded full model (see the deformation of full model, which is shown in Figure 8b). The ratio of the COD to load for the sub-model for  $a = 0.5$  mm was calculated to be  $0.24 \mu\text{m/N}$ , which compares very well to the experimental observations ( $\sim 0.25 \mu\text{m/N}$ ). The horizontal displacement profile, obtained using the sub-model, also shows a much better agreement with the DVC data (compare the blue solid line of FE-sub-model with the dashed green line of DVC measurement in Figure 9a). The ratio of the average COD to CMOD at the surface in the DVC-informed sub-model was 0.86.

The sub-models were then used to establish the relationship between crack depth and COD (Figure 9b). Using the COD data measured via DVC, the crack depths are estimated to be  $a = 0.5 \pm 0.1$  mm and  $a = 0.7 \pm 0.2$  mm for the uniaxial and biaxial conditions. These values compare well with the strain visualisations (Figure 7), confirming that the two defects have similar depths.

## 4 Discussion

The flexural strength of Gilsocarbon nuclear-grade isotropic polygranular graphite has been measured under uniaxial (four-point bend) and equi-biaxial (ring-on-ring) loading. The average bending stress for unstable fracture is reduced by approximately 18% under equi-biaxial stress compared to uniaxial stress. This is consistent with previous observations in isotropic polygranular graphite [11]. The measured strengths fit a Weibull distribution for both conditions, with no significant effect of stress state on the Weibull exponent; this is consistent with the fundamental local approach assumptions (for more details see [22]). The high exponent value suggests a three-parameter Weibull distribution may be a better representation, with a minimum strength threshold that could be sensitive to stress state [22]. This would require further investigation, but with sufficient data might improve forecasting of the probability of failure in different stress states.

Structural integrity assessments of graphite components are carried out with the conservative assumption of linear elasticity (e.g. [18]). A Rankine model was used in an earlier work [21] to develop a local criterion for fracture, predicting only about 7% reduction in the strength of graphite under biaxial loading compared to the uniaxial conditions. There are alternative elastic models that could be used: for instance Beltrami's model predicts an 18% reduction in the equi-biaxial strength of graphite

for Poisson's ratio  $\nu=0.21$ , which is the same as that measured here. The Beltrami model is based on a total strain energy density (SED) model, which has also been used successfully to predict the strength of U and V-notched graphite specimens under mixed mode loading (see [4, 9, 10]).

Digital image correlation was employed to here measure the full-field displacements on the tensile surface of the specimens, thereby observing the sub-critical growth of cracks; crack nuclei were detected when their opening displacements exceeded the measurement noise. Measurements of the crack mouth opening compliance revealed that the crack nuclei tended to open significantly more under equi-biaxial stress in comparison to uniaxial stress (see Figure 4 in which the blue circular symbols show the opening displacement under equi-biaxial loading compared to red triangular symbols for uniaxial loading). If linear elastic properties were assumed, this would imply that deeper crack nuclei were observed under equi-biaxial stress, since although surface crack propagation was observed, the opening compliance of shallow cracks is insensitive to surface crack length. The observations of sub-critical cracks provide no evidence for their propagation in depth: different degrees of such propagation during loading might account for the compliance differences under uniaxial and equi-biaxial stress, but would be inconsistent with the similar depths and compliance of the same cracks on their subsequent loading. This was measured by three-dimensional digital volume correlation (see the 3D visualisations of non-critical cracks depicted in Figure 7), and the crack depths are close to the size of typical stress concentrating defects in the microstructure. It is concluded that the increased crack opening obtained under equi-biaxial stress is due to inelastic strains local to the crack, which are greater under equi-biaxial stress than uniaxial stress. These inelastic strains develop on the first loading of defects in the microstructure; they are most likely due to microcracking

and do not contribute significantly to the crack's compliance when the sample is reloaded.

A novel approach using digital image correlation and finite element simulation was used to calculate the elastic strain energy release rate associated with surface cracks, propagating sub-critically; this provides a direct measurement of their fracture resistance curves using a continuum description of fracture. The microstructure is heterogeneous, and considering the precision of image correlation, it is conceivable that the local energy release rates might be obtained from the displacements of the microstructural features, provided that the images are sufficiently detailed. This is being pursued by the authors, with the aim of resolving the drawbacks of calculating energy release rate by continuum approaches that were discussed recently by Sih [31]. The combination of image correlation and FE is applicable to both energy release rate and local approach methods, such as strain energy density.

The  $J$ -Resistance data show that both the initiation and propagation regions of the  $J$ -Resistance curve are significantly influenced by the stress state (see Figure 5 in which the blue circular symbols show the data under equi-biaxial loading, with red triangular symbols for uniaxial loading); the strain energy release rates, which depend directly on the displacement fields, are greater for equi-biaxial stress than uniaxial stress. The measured difference is significantly greater than might be explained by the expected effects of stress magnitude or stress state on bulk elastic modulus. Sensitivity of the  $J$ -Resistance curve to stress state is classical behaviour for materials that exhibit non-negligible inelastic behaviour; in contrast, fully elastic materials exhibit only weak stress-state sensitivity of fracture toughness [32]. These observations further support the differences in the crack tip inelastic deformation under different states of stress



that were deduced from the crack opening behaviour. A direct relation between the size of the fracture process zone and dissipated energy has been shown for ductile metals such as aluminium alloy [12]. The observed higher work of fracture under equi-biaxial stress in nuclear graphite, measured as a strain energy release rate, is in agreement with increased crack tip inelastic strains.

This effect of stress state might be understood by considering the constraint of a crack under load: in an infinite plate there is no difference for uniaxial or equi-biaxial loading in the crack opening stresses, which are described by the stress intensity factor, but the non-singular term of stress (i.e. the  $T$ -stress [17]) differs significantly between equi-biaxial and uniaxial loading; the crack constraint therefore differs. The biaxiality ratio  $\beta$ , defined below, describes the ratio of the  $T$ -stress to the stress intensity factor  $K$ , and changes at the surface of the tested specimens from -0.95 in the uniaxial condition to -0.04 in the equi-biaxial condition:

$$\beta = \frac{T\sqrt{\pi a}}{K}$$

The  $T$ -stress is an elastic parameter that describes the plastic constraint effect in materials that are able to dissipate energy through unrecoverable inelastic deformation. The response of a crack in a quasi-brittle material, such as polygranular graphite, to an in-plane state of stress might therefore be predicted from its  $T$ -stress. For instance, empirical equations for structural integrity assessments of elastic-plastic materials have been established between the critical  $J$ -integral at different constraint levels and a constraint quantifying parameter such as  $T$ -stress or  $Q$  (see for example [13]). Similarly, since the energy release rate calculated directly from the measured displacement field does not depend on the assumed stress field, an empirical  $J$ - $T$  or  $J$ -

$Q$  fracture assessment diagram could be produced if sufficient data at different constraint levels were obtained by experiment. Such an empirical fracture envelope could support the application of local fracture criteria that were capable of simulating constraint, such as SED, to establish an appropriate local fracture criterion for conditions where no experimental data were available.

It should be noted, however, that for a surface semi-elliptical crack, the nature of constraint differs on the free surface and at its deepest point: on the surface, the equi-biaxial stress field acts to open the crack and to pull it in a direction that is parallel to the crack propagation direction; this in-plane constraint is quantified by the  $T$ -stress [17]. At the deepest point of the crack, on the other hand, the biaxial stress acts to open the crack and to pull it in a direction perpendicular to the crack propagation direction; in this case, the out-of-plane constraint is quantified by the parameter  $T_z$  [33] as the ratio between the out-of-plane normal stress and summation of the other two normal stresses. Although in-plane and out-of-plane constraint have been found to have similar effects on fracture behaviour [12], their influence on the fracture toughness is not qualitatively equivalent [34]; the critical strain energy release rates for unstable propagation may therefore differ with in-plane and out-of-plane constraint. Consequently, no attempt is made here to relate the increase in measured surface strain energy release rates for subcritical crack propagation between uniaxial and equi-biaxial stress to the corresponding decrease in the flexural stress at which unstable fracture occurs. Interpreting this will require a detailed study of the three-dimensional strain fields around short cracks and the unstable crack propagation; these are the subjects of current research.

## 5 Conclusions

- The flexural strength in slender specimens of Gilsocarbon polygranular graphite decreases by 17.8% under equi-biaxial loading compared to the uniaxial loading.
- Digital image correlation, applied to optical observations of the tensile surface, shows that unstable fracture is preceded by the sub-critical propagation of surface cracks: their opening compliance (the ratio of crack mouth opening displacement to stress) was measured to be greatest under equi-biaxial loading. Digital volume correlation and X-ray computed tomography, applied to visualise the crack in 3D within the material, showed cracks developed under uniaxial and equi-biaxial loading to have similar dimensions: the differences in opening compliance are deduced to be due to an effect of stress state on inelastic crack tip deformation.
- A combined digital image correlation and finite element method was used to measure the fracture resistance ( $J$ -integral) of sub-critical cracks: the fracture resistance is greater under equi-biaxial loading. This is consistent with increased inelastic crack tip deformation.
- It is proposed that the effect of stress state on sub-critical cracks in quasi-brittle materials, such as polygranular graphite, may be explained in terms of the plastic constraint effect, described by the relationship between the applied loading and the  $T$ -stress component of the crack tip stress field.

## Acknowledgement

T.J. Marrow and M. Mostafavi acknowledge the support of the Oxford Martin School and EDF Energy (GRA/GNSR/6041). The opinions expressed are those of the

authors and not necessarily those of EDF Energy. We acknowledge funding from the EPSRC for the X-ray imaging facility under EP/F007906/1 and EP/F028431/1. M. Mostafavi also acknowledges the support of Linacre College, Oxford, through a Junior Research Fellowship. H. Cetinel thanks Higher Education Council of Turkey (YÖK) for the financial support during his visit to the Oxford University. The authors would also like to thank the EPSRC engineering instrument pool, Mr Peter Anthony and Mr Adrian Walker, for providing us with the high-speed camera.

## References

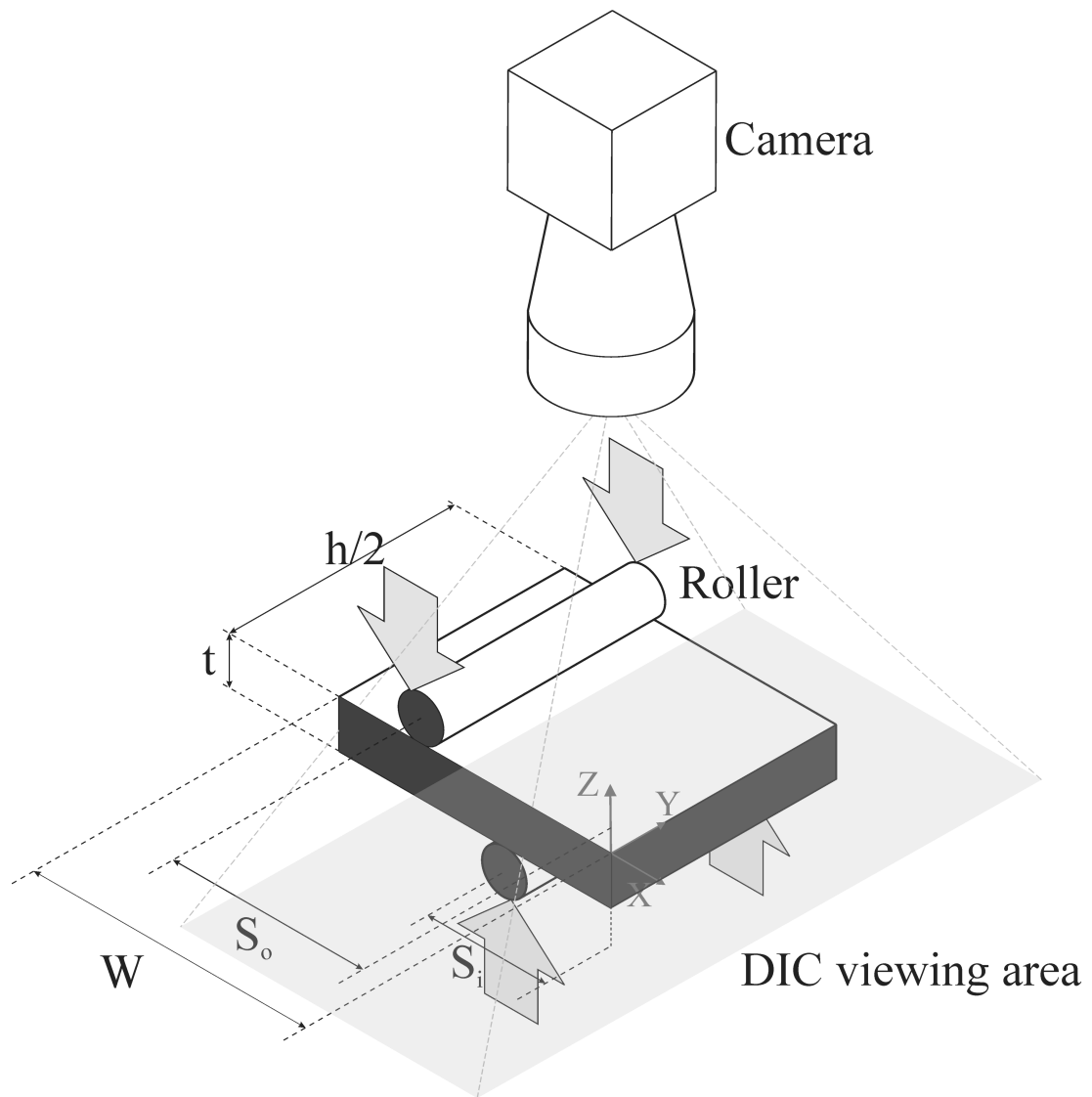
- [1] Hodgkin AD, Marrow TJ, Wootton MR, Moskovic R, Flewitt PEJ. Fracture behaviour of radiolytically oxidised reactor core graphites: a view. *Mater Sci Technol.* 2010;26(8):899-907.
- [2] Arnould M, Baeten F, Darquennes D, Delbar T, Huyse M, Jongen Y, et al. Target development for a radioactive ion beam. *Nucl Instrum Methods Phys Res Sect A-Accel Spectrom Dect Assoc Equip.* 1989;A282:99-101.
- [3] Emley EF. Continuous casting of aluminium. *Int Met Rev.* 1976;21:75-115.
- [4] Ayatollahi MR, Berto F, Lazzarin P. Mixed mode brittle fracture of sharp and blunt V-notches in polycrystalline graphite. *Carbon.* 2011;49(7):2465-74.
- [5] Burchell TD. A microstructurally based fracture model for polygranular graphites. *Carbon.* 1996;34(3):297-316.
- [6] Boey SY, Bacpn DJ. Bend strength of graphite under pressure. *Carbon.* 1986;24(5):571-4.
- [7] Brocklehurst JE. Fracture in polycrystalline graphite. *Chem Phys Carb.* 1977;13:145-63.

- [8] Tsang DKL, Marsden BJ. The development of a stress analysis code for nuclear graphite components in gas-cooled reactors. *J Nucl Mater.* 2006;350(3):208-20.
- [9] Berto F, Lazzarin P, Ayatollahi MR. Brittle fracture of sharp and blunt V-notches in isostatic graphite under torsion loading. *Carbon.* 2012;50:1942-52.
- [10] Berto F, Lazzarin P, Marangon C. Brittle fracture of U-notched graphite plates under mixed mode loading. *Mater Des.* 2012;41:421-32.
- [11] Burchell TD, Yahr GT, Battiste R. Modelling the mutiaxial strength of H-451 nuclear grade graphite. *Carbon.* 2007;45(13):2570-83.
- [12] Mostafavi M, Smith DJ, Pavier MJ. Reduction of measured toughness due to out-of-plane constraint in ductile fracture of aluminium alloy specimens. *Fatigue Fract Eng Mater Struct.* 2010;33(1):724-39.
- [13] R6. Assessment of the Integrity of Structures Containing Defects: British Energy; 2001.
- [14] Brocks W, Schmitt W. Second parameter in J-R curves: constraint or triaxiality? . *Constraint effects in fracture: Theory and application.* Dallas, TX, USA; 1993.
- [15] Karihaloo BL. *Fracture Mechanics and Structural Concrete.* New York: Longman Scientific and Technical Publishers; 1995.
- [16] Sherry AH, Wilkes MA, Beardsmore DW, Lidbury DPG. Material constraint parameters for the assessment of shallow defects in structural components - Part I: Parameter solutions. *Eng Fract Mech.* 2005;72:2373-95.

- [17] Larsson SG, Carlsson AJ. Influence of non-singular stress terms and specimen geometry on small-scale yielding at crack tips in elastic-plastic materials. *J Mech Phys Solids*. 1973;21:263-77.
- [18] Ho FH. Graphite design handbook. San Diego, CA: General Atomics; 1988.
- [19] Ouagne P, Neighbour GB, McEnaney B. Crack growth resistance in nuclear graphites. *JOURNAL OF PHYSICS D: APPLIED PHYSICS*. 2002;35:927-34.
- [20] Becker TH, Mostafavi M, Tait RB, Marrow TJ. An Approach to Calculate the J-Integral by Digital Image Correlation Displacement Field Measurement Fatigue Fract Eng Mater Struct. 2012;35:971-84.
- [21] Mostafavi M, Marrow TJ. In situ observation of crack nuclei in poly-granular graphite under ring-on-ring equi-biaxial and flexural loading. *Eng Fract Mech*. 2011;78(8):1756-70.
- [22] Rosahl K, Booker JD, Lewis S, Smith DJ. A statistical approach for transferring fracture events across different sample shapes. *Eng Fract Mech*. 2011;78:47-59.
- [23] DaVis. User's Manual. Gottingen: LaVision GmbH,; 2009.
- [24] Mostafavi M, Marrow TJ. Quantitative in-situ study of short crack propagation in polygranular graphite by digital image correlation. *Fatigue Fract Eng Mater Struct*. 2012;35(8):695-707.
- [25] Hild F, Roux S. Measuring stress intensity factors with a camera: Integrated image correlation (I-DIC). *Comptes Rendus de l'Academie des Sciences Serie II b/Mecanique*. 2006;334:8-12.

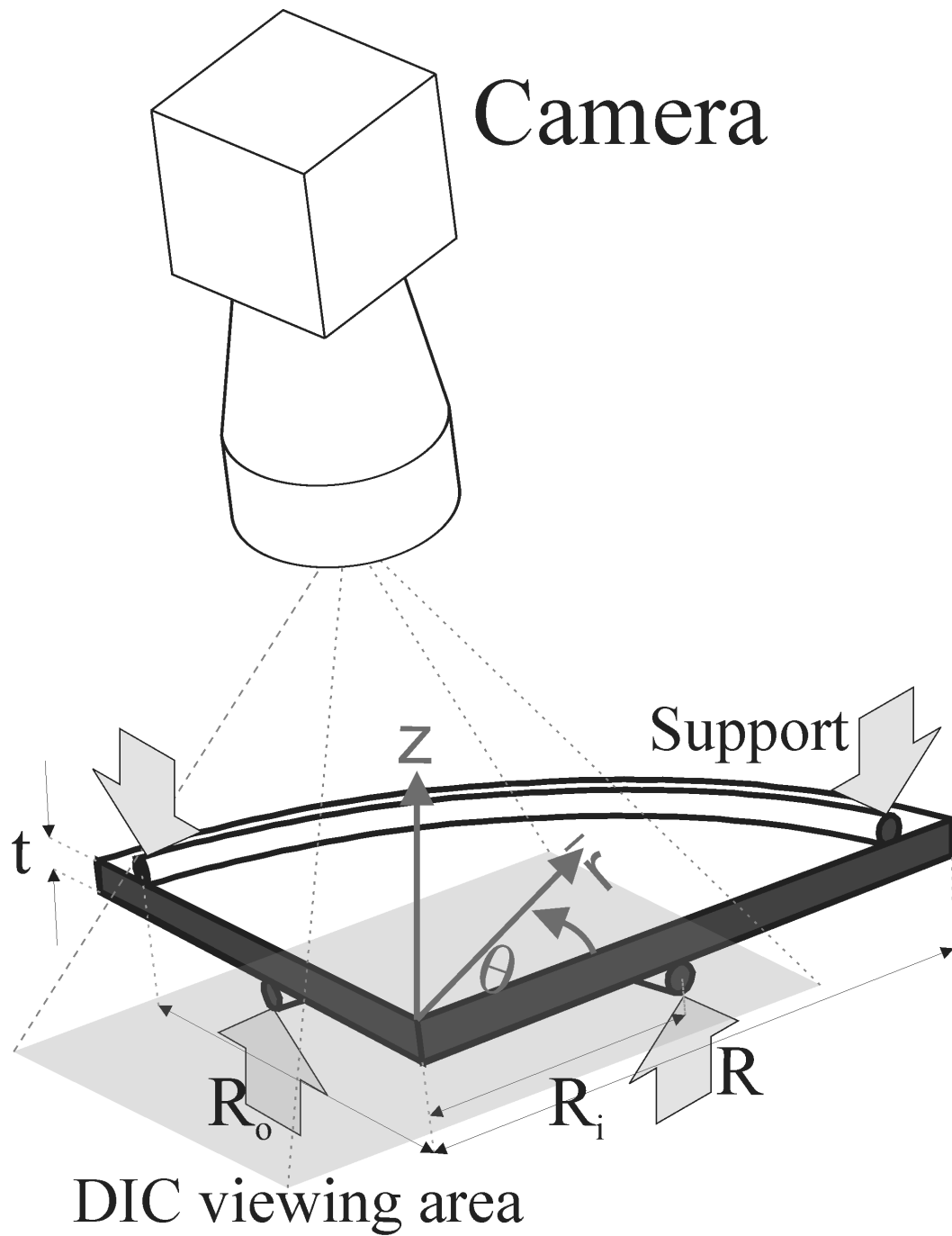
- [26] Mostafavi M, McDonald SA, Mummery PM, Marrow TJ. Observation and quantification of three-dimensional crack propagation in poly-granular graphite. Eng Fract Mech. 2012;<http://dx.doi.org/10.1016/j.engfracmech.2012.11.023>.
- [27] Sato S, Awaji H, Kawamata K, Kumrumada A, Oku T. Fracture criteria of reactor graphite under multiaxial stresses. Nucl Eng Des. 1987;103:291-300.
- [28] Mostafavi M, Schmidt M, Marsden BJ, Marrow TJ. Fracture behaviour of an anisotropic polygranular graphite (PGA) Mater Sci Eng, A. 2012;558(15):265-77.
- [29] Joyce MR, Marrow TJ, Mummery PM, Marsden BJ. Observation of microstructure deformation and damage in nuclear graphite. Eng Fract Mech. 2008;75(2):3633-45.
- [30] DaVis. User's Manual. Gottingen: LaVision GmbH,; 2012.
- [31] Sih GC. Efficacy of invariant surface energy density for multiscale shifting of volume energy density. Theor Appl Fract Mech. 2013;In Press.
- [32] Chao YJ, Liu S, Broviak BJ. Brittle fracture: Variation of fracture toughness with constraint and crack curving under mode I conditions. Exp Mech. 2001;41(3):232-41.
- [33] Guo W. Elastoplastic three dimensional crack border field - I. Singular structure of the field. Eng Fract Mech. 1993;46(1):93-104.
- [34] Mostafavi M, Smith DJ, Pavier MJ. Fracture of aluminium alloy 2024 under biaxial and triaxial loading. Eng Fract Mech. 2011;78(8):1705-16.

## Figures



(a)





(b)

Figure 1 – Overview of experiment geometries; (a) one quarter of the uniaxial four point bend test, (b) one quarter of the equi-biaxial ring-on-ring test. The symmetry planes are shaded dark grey

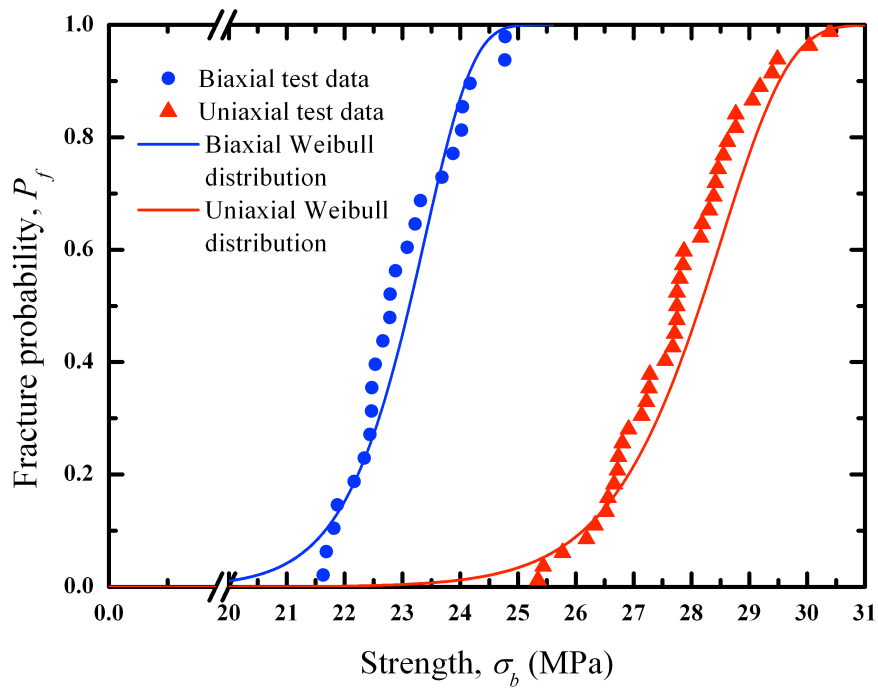
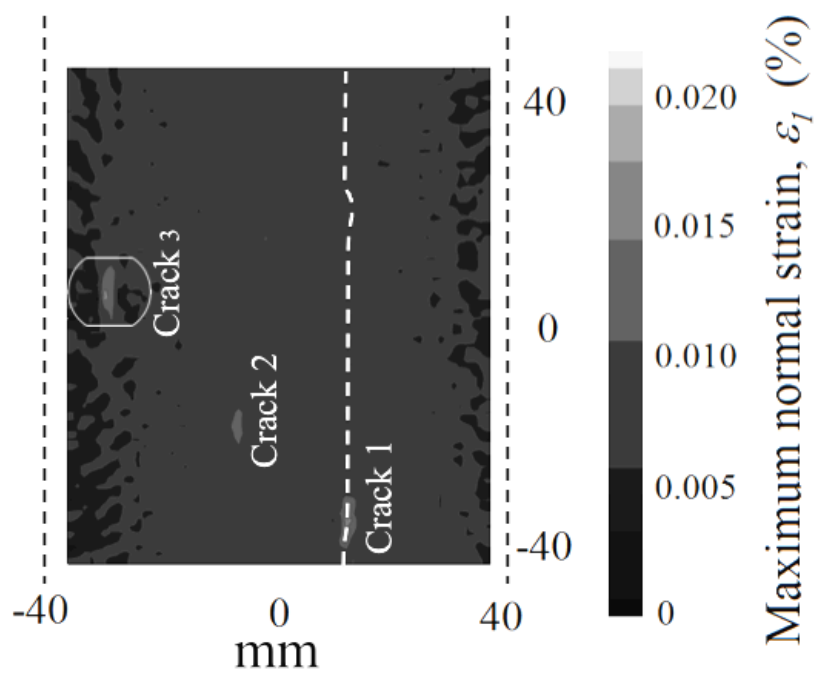
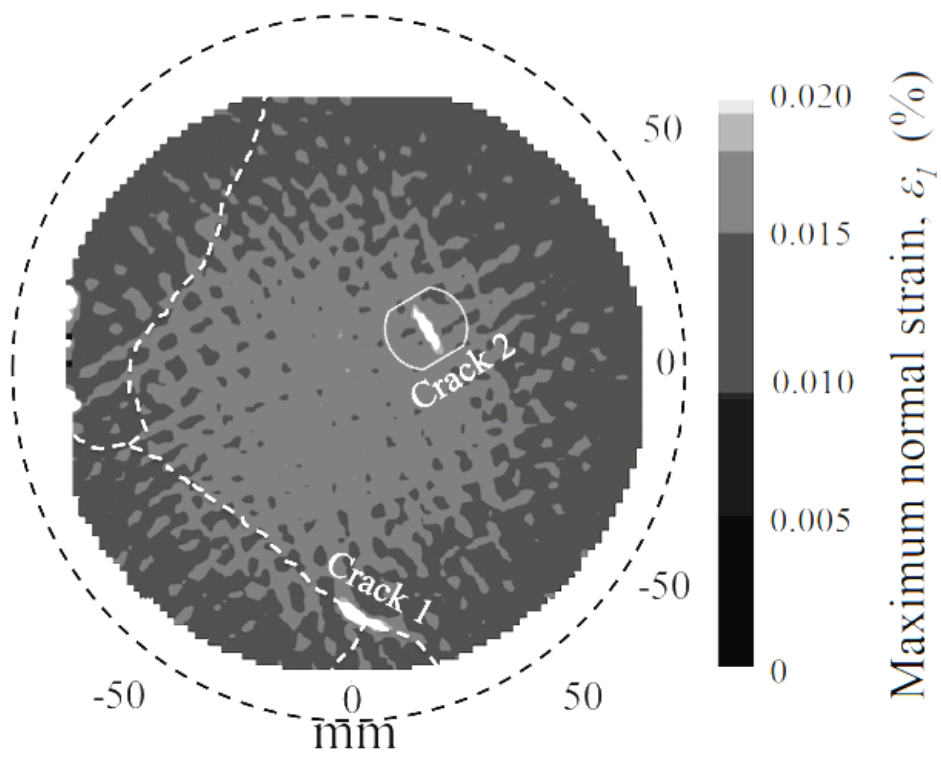


Figure 2 – Two-parameter Weibull distribution representation of the flexural strength of graphite. Under uniaxial load:  $\sigma_w=28.56$  MPa,  $m=25.27$ ; equi-biaxial load:  $\sigma_w=23.43$  MPa,  $m=25.36$



(a)



(b)

Figure 3 – Example of the deformation fields, visualised as nominal strains for (a) uniaxial and (b) equi-biaxial loading. The dark dashed line shows the position of the inner support. Light grey patches of high strain indicate cracks; the white dashed line shows the path of the propagated critical crack, which caused catastrophic failure. The samples cut (see Figure 6) for further studies are illustrated around the identified non-critical cracks.

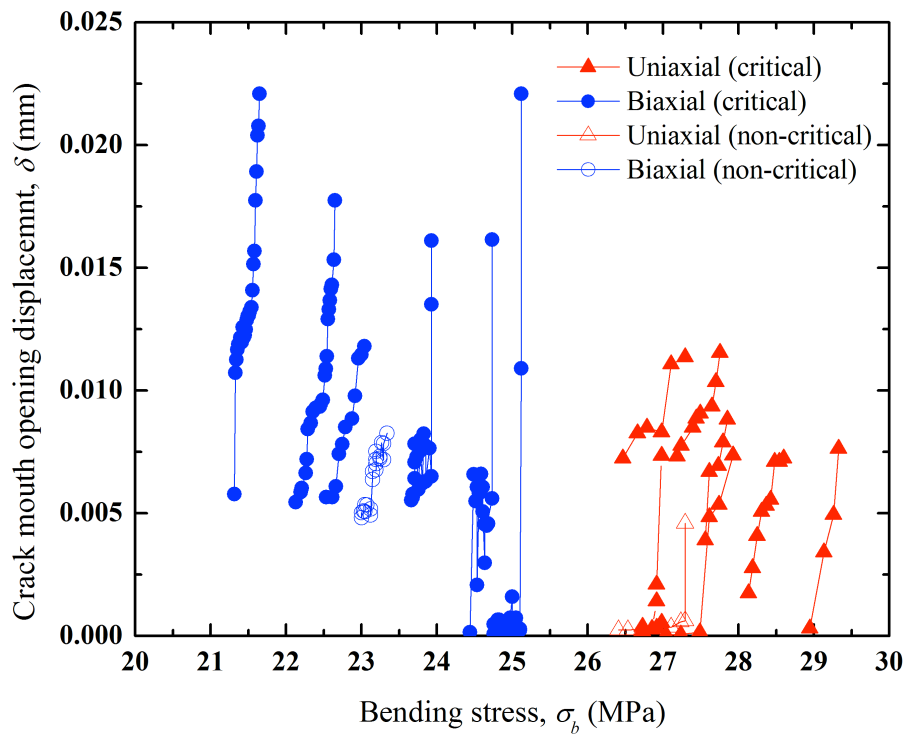


Figure 4 – Crack mouth opening displacement calculated by digital image correlation analysis. Critical cracks are those that transitioned to unstable propagation; all the measurements were made during sub-critical propagation. The non-critical cracks are those identified in Figure 3.

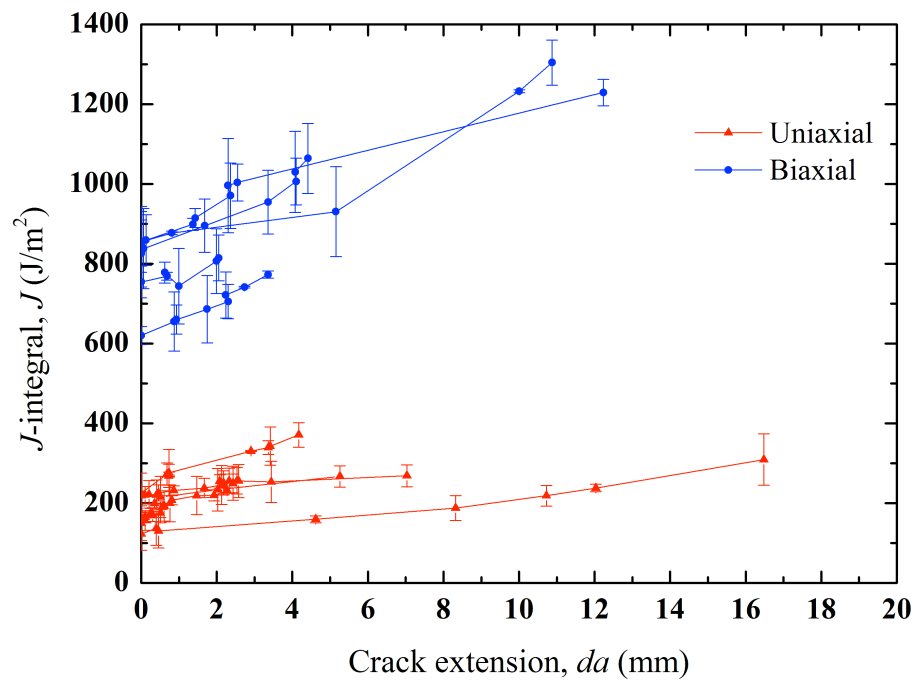
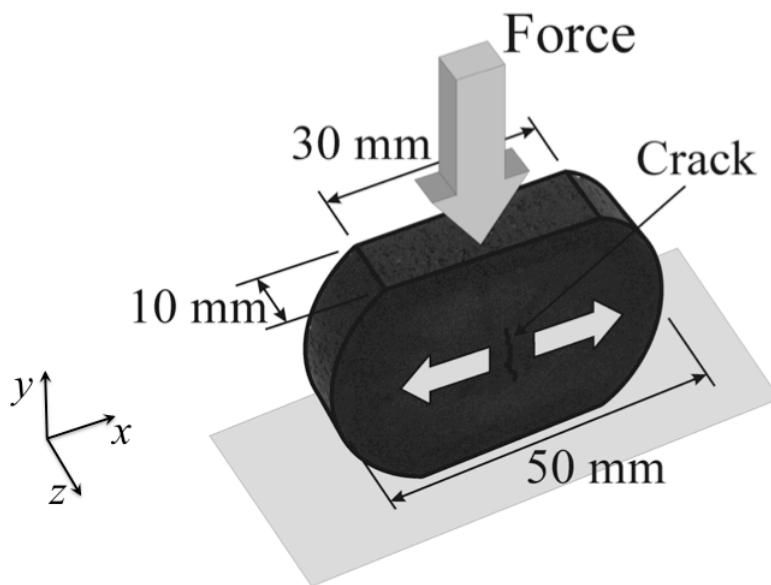
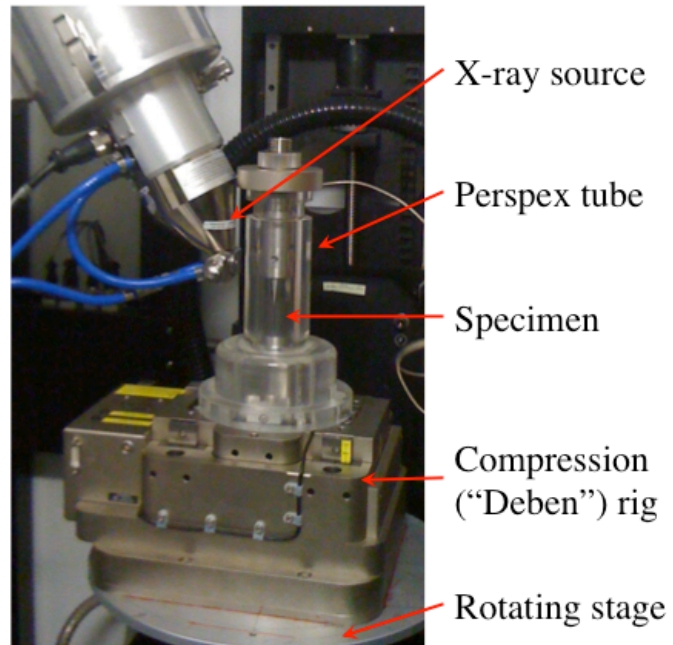


Figure 5 - Resistance curve of crack nuclei under uniaxial and equi-biaxial loading.

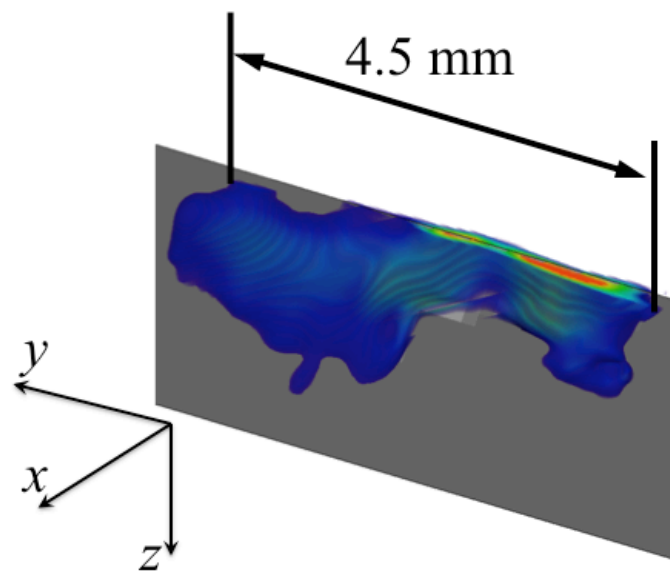


(a)

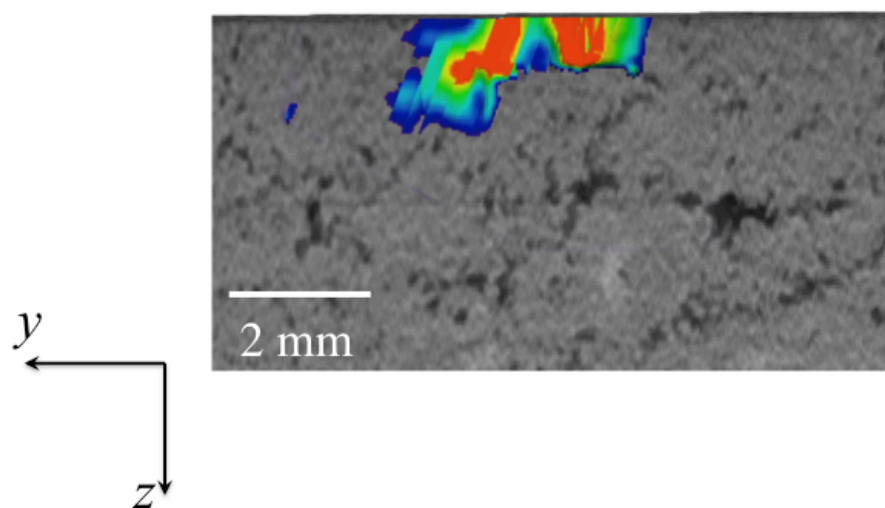


(b)

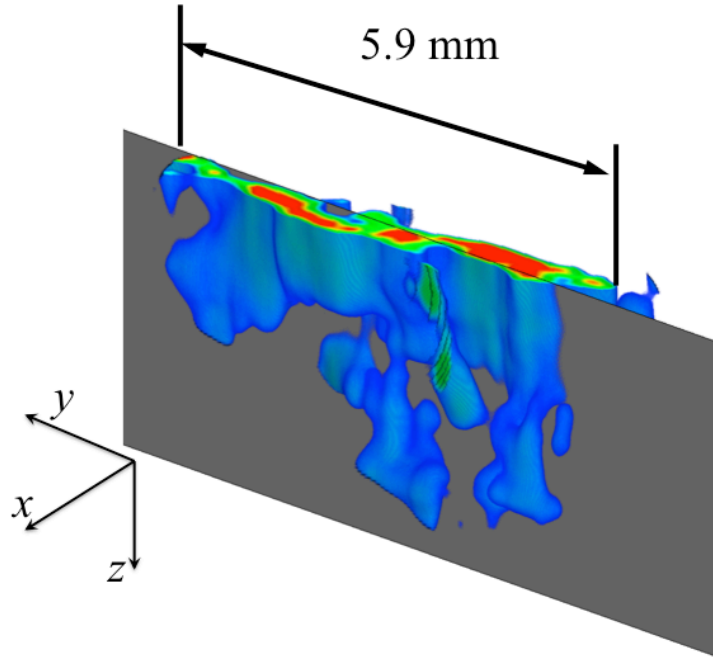
Figure 6 – Tomography experiment; (a) cut sample (flat Brazilian disc) containing a non-critical crack, (b) setup of the in-situ compression rig in the X-ray chamber



(a)



(b)



(c)

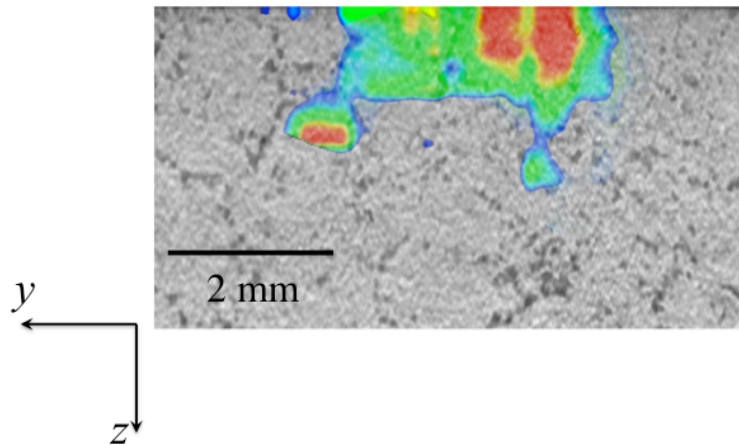
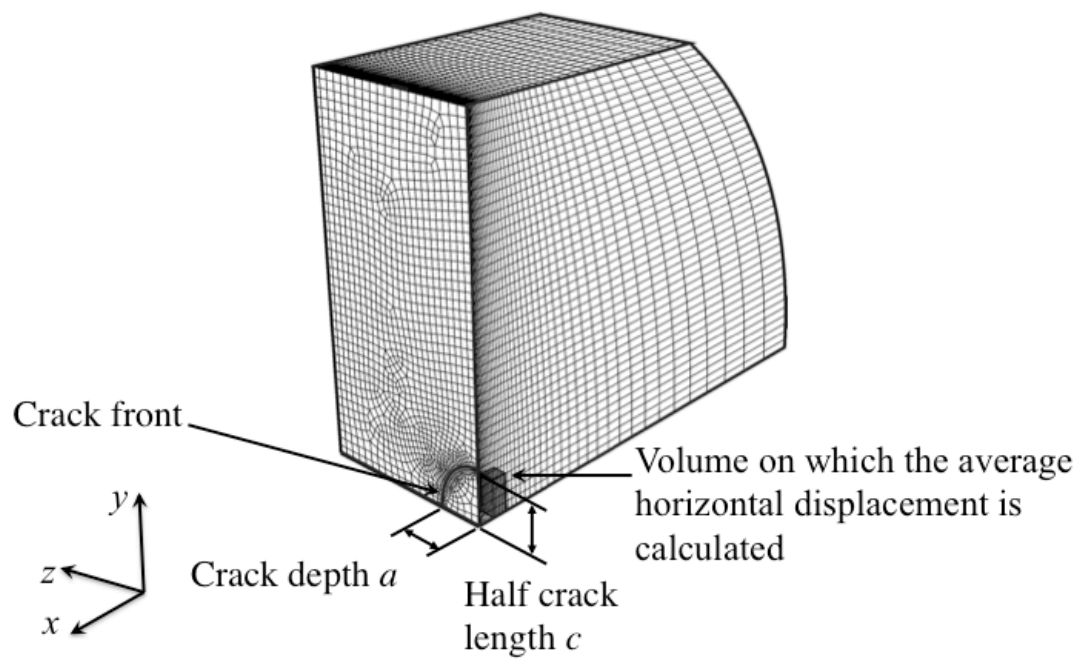
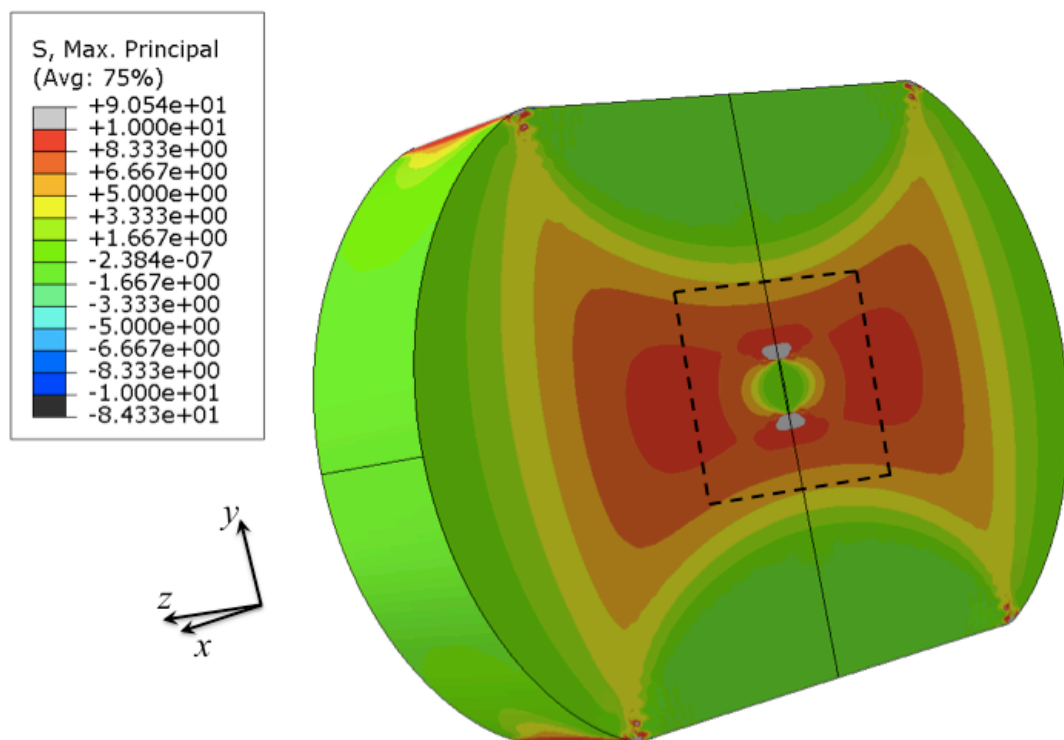


Figure 7 – 3D visualisation of the non-critical cracks using the measured nominal strain field; (a) crack initiated under uniaxial load, and (b) its relation with microstructure; (c) crack initiated under equi-biaxial load, and (d) its relation with microstructure – the positions of the image slices shown in (b) and (d) are marked in (a) and (c) as shaded planes.

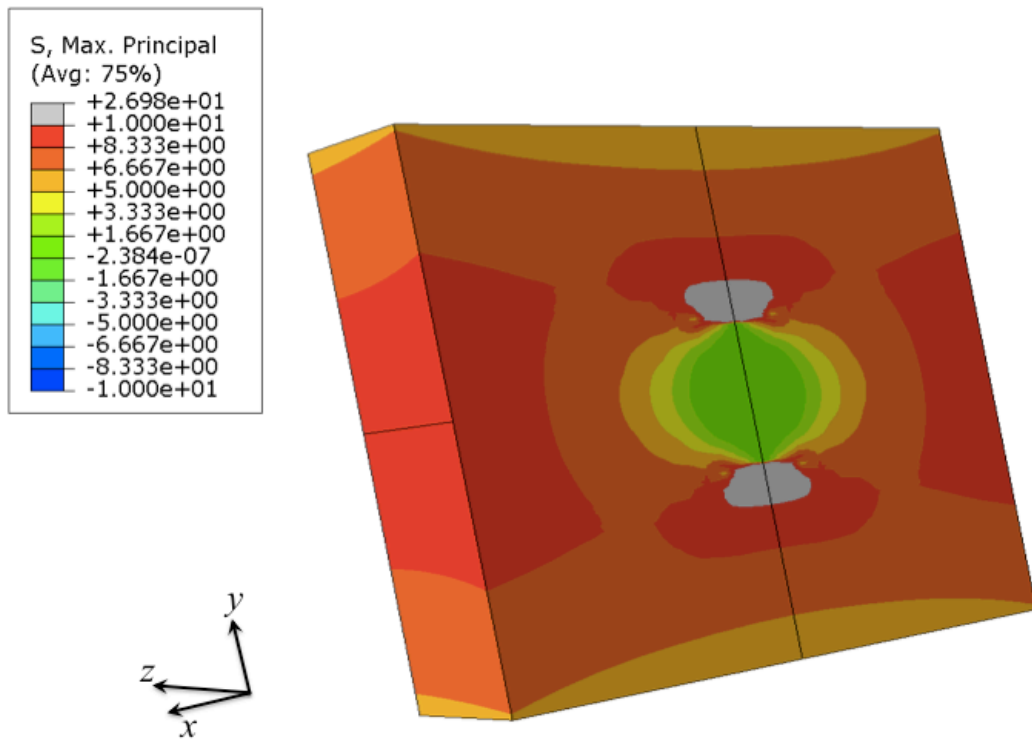




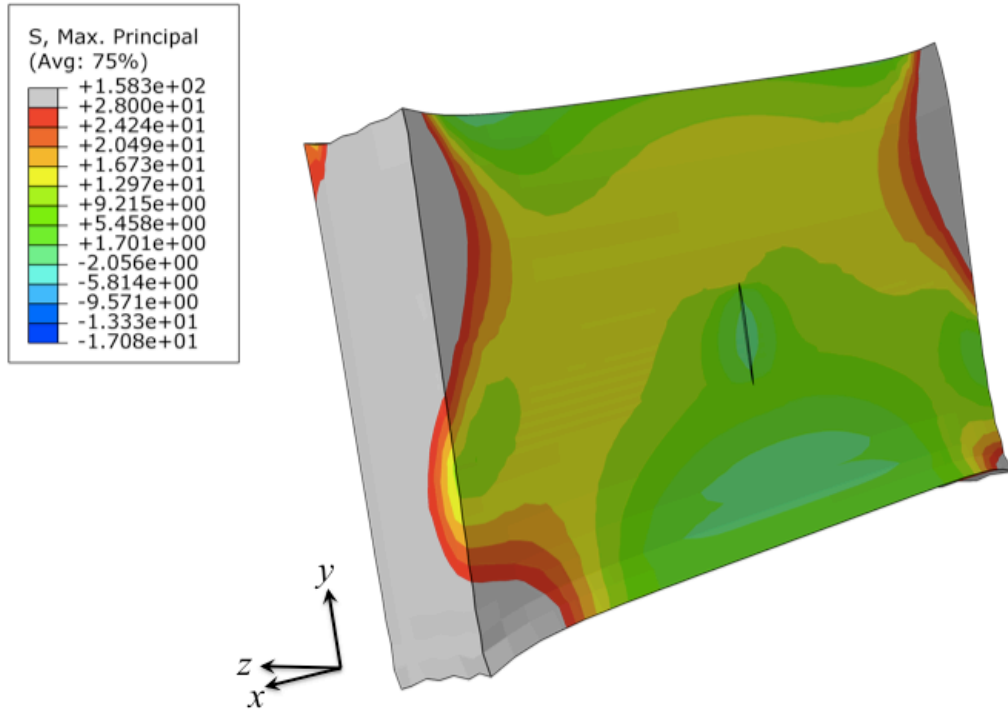
(a)



(b)

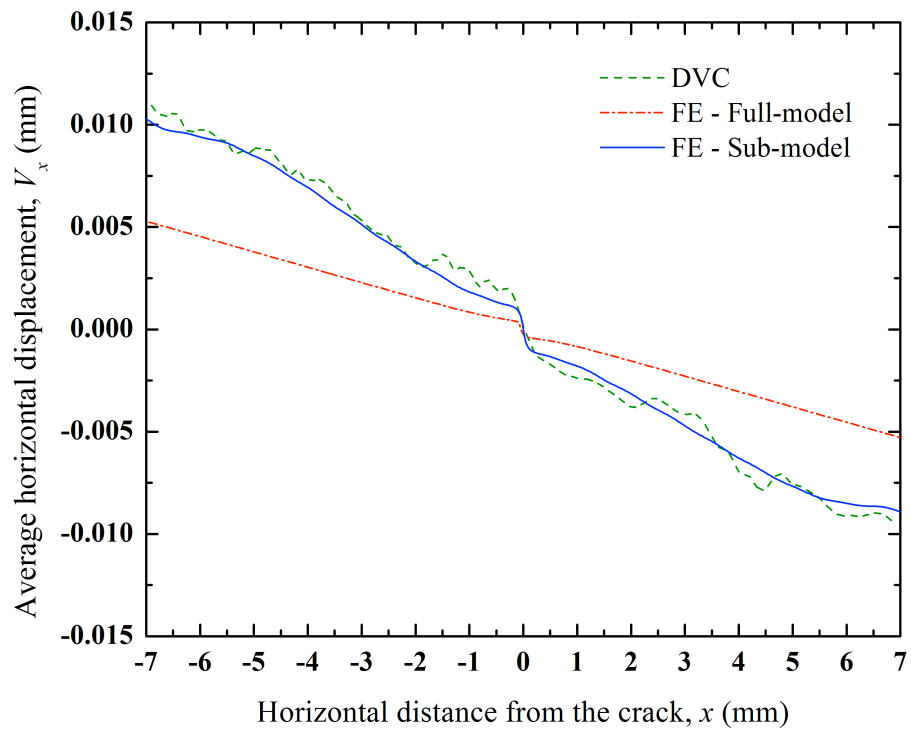


(c)

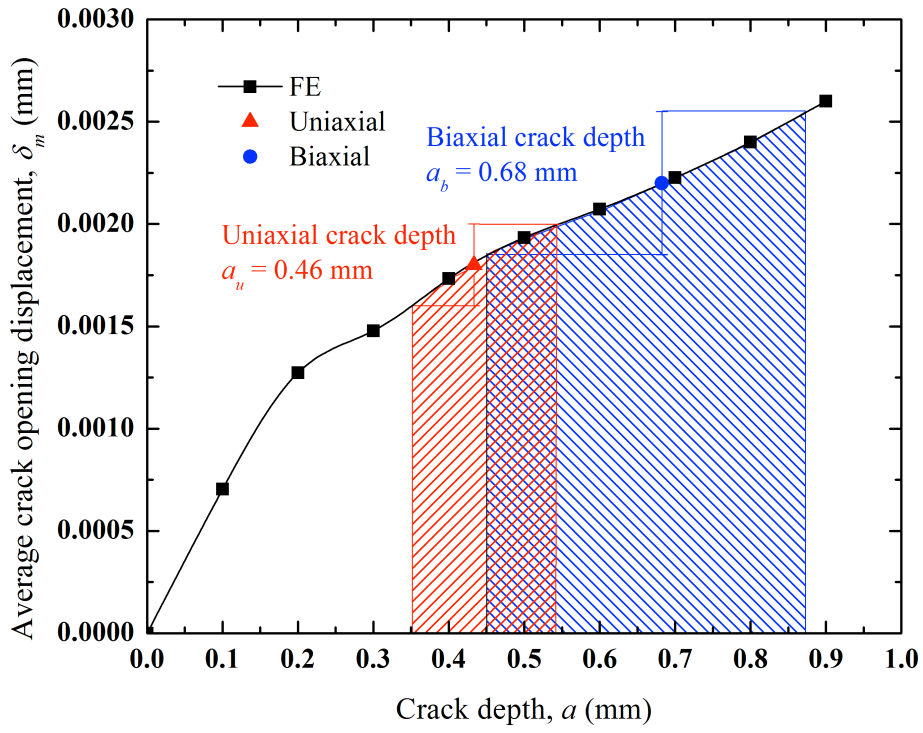


(d)

Figure 8 – Finite element simulation; (a) Overview of one quarter of the full model FE mesh for the specimen with a semi-elliptical crack, (b) deformation of the full-model under ideal uniform loading, the region corresponding to the sub-model is marked with dashed line and is magnified in (c), the deformed DVC-informed sub-model is shown in (d). The deformations in (b), (c) and (d) are magnified 25 times.



(a)



(b)

Figure 9 – (a) the distribution of average horizontal displacement, compared with the experimental data, (b) the variation of average crack opening displacement with crack depth from the FE sub-model analysis, and the estimation of crack depth from measured compliance.